Compensation of the tool influence function changes under neighborhood effect in atmospheric pressure plasma processing

PENG JI,[1,2,3,4] DUO LI,[1,2,*] YUAN JIN,[1] XING SU,[5] AND BO WANG[1]

[1] *Center for Precision Engineering, Harbin Institute of Technology, Harbin 150001, China*
[2] *Changchun Institute of Optics, Fine Mechanics and Physics, Chinese Academy of Sciences, Changchun 130033, China*
[3] *Key Laboratory of Optical System Advanced Manufacturing Technology, Chinese Academy of Sciences, Changchun 130033, China*
[4] *State Key Laboratory of Applied Optics, Changchun 130033, China*
[5] *Sichuan Precision and Ultra-Precision Machining Engineering Technology Center, Chengdu 610200, China*
liduo@hit.edu.cn

Abstract: Nowadays, computer controlled optical surfacing (CCOS) is greatly developed in the fabrication of ultra-precision optical surfaces. As one of the deterministic CCOS techniques, atmospheric pressure plasma processing (APPP) can achieve the efficient removal based on the chemical reaction. In this process, the temperature rising issue caused by plasma heating is of great importance for accelerating the etching rate, but also increases the difficulty of deterministic removal control, because the tool influence function (TIF) in APPP is no longer time-invariant. In the existing research, the time-variant TIF model can describe the TIF changes to a certain degree, which is considered in the dwell time calculation. However, there inevitably exists the strong neighborhood effect, which indicates that the TIFs of different dwell points are thermally interacted. Thus, the existing time-variant TIF model is no longer accurate for predicting TIF changes, and not suitable for application to further compensation. To solve this, the compensation of TIF changes under neighborhood effect is proposed in this paper. First, the mechanism of TIF changes caused by neighborhood effect is explained in depth. Then, the theoretical analysis is implemented and the compensation method is systematically discussed, encompassing the tool path optimization, model of TIF changes and dwell time calculation. Further, the proposed method is demonstrated and verified by a series of simulations. Finally, the experimental validation is carried out, which proves the capability of achieving high-precision removal and high convergence rate.

1. Introduction

In recent years, computer controlled optical surfacing (CCOS) technology is greatly developed, which is driven by its increasing applications in the fabrication of optical components with high-precision surface quality [1]. Many advanced polishing methods [2–5] have shown the flashes of brilliance in the figuring or superfine finishing of optical surface.

As one of the non-conventional deterministic processing methods, the atmospheric plasma processing technology has shown the unique superiority for structuring [6] and figuring of optical components [7]. Excited by the radio frequency (RF) power, the fluorine-based plasma jet is generated and impinged on the optical surface, which achieves material removal through the chemical reaction introduced by the reactive particles in plasma jet [8,9]. The principle of pure chemical etching makes this technique extremely competitive for the high-precision optical fabrication with high efficiency, no damage and low cost. For better understanding its removal

characteristics and application, many researchers have thoroughly studied the homogeneous technologies, such as reactive atom plasma technology (RAPT) [8], plasma jet machining (PJM) [9], plasma chemical vaporization machining (PCVM) [10], arc-enhanced plasma machining (AEPM) [11] and atmospheric pressure plasma processing (APPP) [12].

For the CCOS essence of atmospheric plasma figuring or structuring, the tool influence function (TIF) constancy between the simulation analysis and actual processing is of great importance during the dwell time calculation for the high convergence rate. However, this goal is difficult to achieve because of the thermal effect generated by the plasma jet. For other CCOS tools [13–15], the TIF keeps theoretically unchanged, which is matched with the assumption of unchanged TIF in the conventional deconvolution algorithms [16]. As for the atmospheric plasma processing technology, the substrate temperature is not stable and constantly changed based the execution of the dwell time map. Further, the TIF also changes with the temperature [7,17], which poses great challenges to the high-precision removal control. Therefore, the compensation of TIF changes becomes the research hotspot in the atmospheric plasma processing technique.

In recent years, the similar TIF changes issue has attracted the attention of scholars, such as the curvature effect on TIF changes [18], and the generic model of time-variant TIF and dwell-time algorithm was proposed [19]. However, these theories are not successfully applied to the atmospheric plasma processing technique. To address this issue, Meister et al. [20] established the thermal model to simulate the spatio-temporal temperature field of substrate during PJM process. Based on this, the absolute surface topography occurring after PJM can be precisely simulated by further calculating the temperature-dependent local material removal rate function. This method is indeed accurate, but costs a large number of valuable time and high hardware cost. To simplify the procedure, many researchers paid attention to the mapping relationship between the dwell time and transient temperature. By implementing the multiple scanning test with different constant velocities, the time-variant TIF model can be established and considered in the calculation of the dwell time map. Based on this, we presented the optimization strategy for TIF nonlinearity considering the velocity distribution [7]. This method aims at calculating the optimized dwell time map considering the time-variant TIF while keeping the principle of conventional deconvolution procedure. It draws on the statistical idea, and is intended to guarantee the maximum constancy between the calibrated and actual TIFs. The outstanding advantage is the applicability for the figuring of large-aperture optics because of its simplicity. However, the time-variant TIF model is not comprehensively incorporated. Afterward, Su et al. [17,21] proposed the nonlinear dwell time algorithm based on an innovative concept of controlling local volumetric removal (LVR). In the dwell time calculation stage, the complex nonlinear convolution is decoupled into a linear process and a nonlinear process, which is highly effective to be conducted. This method has been successfully applied to the freeform surface generation in the experiment.

Although great strides have been made in the compensation methods of TIF changes for all kinds of atmospheric plasma processing technologies, the neighborhood effect is still not taken into consideration, which makes the complexity of TIF changes far beyond the expectations. In our previous research of APPP, the neighborhood effect was intensively investigated through an innovative reverse analysis method [22], indicating that the TIF of any specific dwell point is not self-determined and thermally connected with the neighboring dwell points. In another word, the temperature-dependent removal characteristic cannot be accurately represented by the existing time-variant TIF model acquired under simple processing condition, not to mention the further compensation.

In this paper, the compensation methodology of TIF changes under neighborhood effect in APPP is proposed, which enhances the removal controllability and improves the convergence rate of single processing. Its advantages lie in not only the high precision of calculation considering neighborhood effect but also the high efficiency and feasibility in application. The rest of the

paper is organized as follows. The mechanism of TIF changes under neighborhood effect is first explained in Section 2. Then, the compensation method is presented in Section 3. Further, the proposed method is demonstrated and verified by a series of simulations in Section 4. Finally, the experimental validation is conducted with the fabrication of freeform surface, which proves its applicability and feasibility.

2. Mechanism explanation of TIF changes under neighborhood effect

In APPP, the reactive fluorine-based plasma jet is generated by plasma torch, which is the key prerequisite of achieving stable and reliable TIFs. In detail, the plasma jet plays two roles, as shown in Fig. 1. First and foremost, the excited plasma jet provides the highly reactive particles that diffuse to the substrate surface, which lays the foundation for chemical reaction, as shown in Fig. 1(a). Meanwhile, the plasma jet can be considered as the heat source, and constantly heats the reaction zone, as shown in Fig. 1(b). Therefore, the TIF is finally codetermined by the distribution of reactive particles and processing temperature.
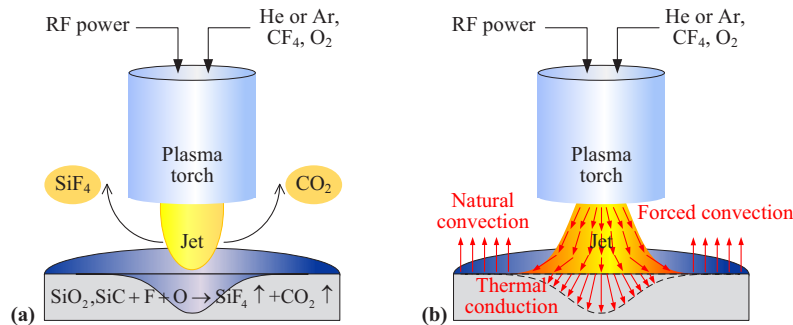

Fig. 1. Two roles of the plasma jet in APPP. (a) Provider of reactive particles. (b) Heat source.

As long as the plasma jet is stably excited and impinged on the substrate surface, the distribution of reactive particles is determined and independent of different dwell positions. When the technological parameters (such as gas flow, power and processing distance, etc) are maintained, the TIF in APPP is greatly influenced by the processing temperature. Therefore, the longer dwell time indicates the higher removal rate of TIF, because the longer heating time leads to the higher processing temperature. However, in practical, the transient processing temperature of any dwell point is not independent of others, which is the crux of neighborhood effect.

Figure 2 gives the schematic of the processing result after the plasma jet dwells at single point. After the impinging jet that carries reactive particles is generated on the substrate surface, the heat flux is input through forced convection. Because the smaller sampling distance is preferred to guarantee the removal continuity, the impinging jet covers more than one dwell point. This way, multiple dwell points (red) are directly heated even if the plasma jet only dwells at single point. Besides, some extra dwell points (green) are also passively heated through the thermal conduction. Finally, the thermal affected area is larger than the effectively processed area ($D_a > D_p$). Based on this phenomenon, the transient processing temperature of any dwell point during processing is not self-determined. For example, it is assumed that the moment in Fig. 2 happens in the left-to-right processing. When the plasma jet dwells at point G, the following points from H to K are also preheated simultaneously and has different initial temperatures. Similarly, the transient processing temperature of point G is also influenced by a series of previous points. Further, the TIF of any specific dwell point is also affected by the multiple preheating effect, which leads to the TIF changes under neighborhood effect.
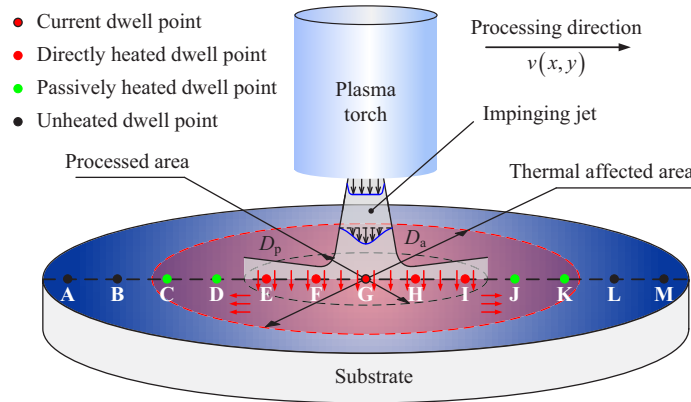
Fig. 2. Schematic of the processing result after the plasma jet dwells at single point.

3. Theoretical analysis and method

3.1. Compensation methodology

Due to the self-heating phenomenon, the TIF changes under neighborhood effect in APPP inevitably appears in the whole processing. To achieve the precise removal control, the processing temperature changes should be incorporated in the TIF to modify the conventional convolution theorem. Therefore, the compensation method of TIF changes should start from the analysis of temperature filed.

If the plasma jet dwells at the first point (x_1, y_1) with the dwell time t_1, the transient temperature field can be expressed as,

$$T(x, y, t_1) = T(x - x_1, y - y_1, t_1^{\text{up}}) \tag{1}$$

In Eq. (1), t_i^{up} represents the heating time of ith point. Similarly, the cooling time is described using t_i^{down} in the following equations. After the transition to the second dwell point, the substrate has been heated, and the transient temperature field at the second dwell point (x_2, y_2) is expressed as,

$$T(x, y, t_1 + t_2) = T(x - x_2, y - y_2, t_2^{\text{up}}) + T(x - x_1, y - y_1, t_1^{\text{up}} + t_2^{\text{down}}) - T_0 \tag{2}$$

In the above and following equations, T_0 is the initial temperature before processing. It's worth noting that the signs of plus and minus are only adopted for qualitative analysis. It does not mean that the temperature fields can be numerically superimposed. Further, the transient temperature field at the third dwell point (x_3, y_3) is expressed as,

$$T(x, y, t_1 + t_2 + t_3) = T(x - x_3, y - y_3, t_3^{\text{up}}) + T(x - x_2, y - y_2, t_2^{\text{up}} + t_3^{\text{down}})$$
$$+ T(x - x_1, y - y_1, t_1^{\text{up}} + t_2^{\text{down}} + t_3^{\text{down}}) - 2T_0 \tag{3}$$

By summarizing regularity, the transient temperature field at the Nth dwell point (x_N, y_N) is expressed as,

$$T\left(x, y, \sum_{j=1}^{N} t_j\right) = T(x - x_N, y - y_N, t_N^{\text{up}})$$
$$+ \sum_{i=1}^{N-1} T\left(x - x_{N-i}, y - y_{N-i}, t_{N-i}^{\text{up}} + \sum_{k=N-i+1}^{N} t_k^{\text{down}}\right) - (N - 1)T_0 \tag{4}$$

Therefore, the transient processing temperature of dwell point (x_N, y_N) can be calculated by Eq. (4) as,

$$T\left(x_N, y_N, \sum_{j=1}^{N} t_j\right) = T(0, 0, t_N^{\text{up}}) + \sum_{i=1}^{N-1} T\left(x_N - x_{N-i}, y_N - y_{N-i}, t_{N-i}^{\text{up}} + \sum_{k=N-i+1}^{N} t_k^{\text{down}}\right) - (N-1)T_0$$

(5)

According to Eq. (5), the transient processing temperature of any specific dwell point is codetermined by multiple influence factors, which should be taken into account in the compensation of TIF changes under neighborhood effect.

Dwell time of multiple dwell points. The first and second terms on the right side of Eq. (5) both contains the dwell time. For the current dwell point (x_N, y_N), its transient processing temperature is predominantly self-determined according to the heating time t_N^{up}. However, the initial temperature has been determined by the dwell time of previous dwell points. The larger value of t_{N-i}^{up} indicates the more significant preheating effect.

Tool path type. In the second term on the right side of Eq. (5), the relative distance $(x_N - x_{N-i}, y_N - y_{N-i})$ and cooling time t_k^{down} suggest the importance of tool path type, which affect the execution order of dwell time. The relative distance describes how far the current dwell point is from other dwell points. The closer the previous dwell point is to the current dwell point, the more significant the preheating effect. However, if one dwell point is close to the current dwell point but cooled for a longer time, its preheating effect on the current point may be greatly weakened because of the prior execution. For example, the influence of tool path type is illustrated in Fig. 3, which includes the raster path and random path. All the discrete grids share the same dwell time map but different tool path. For the current dwell point B4, it is obvious the preheating effect from dwell point B3 is more significant in the raster path.
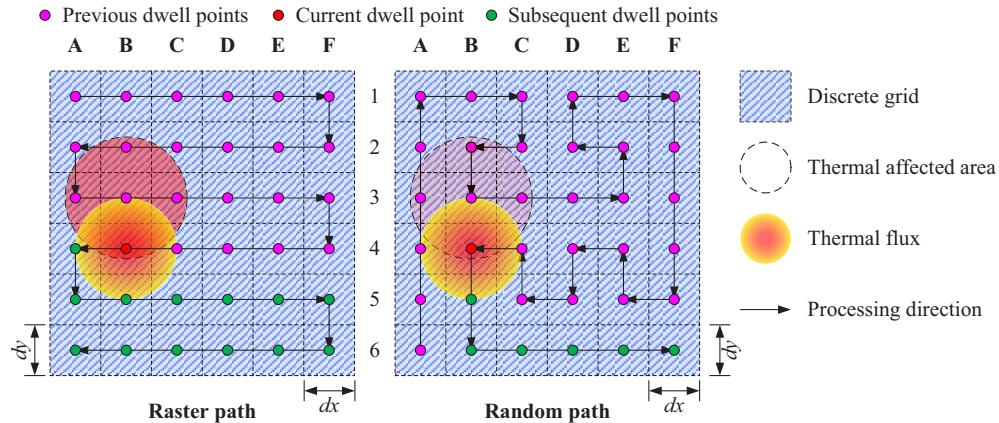

Fig. 3. Influence of the tool path type.

Dwell time calculation. Regarding to the TIF changes under neighborhood effect, the conventional dwell time calculation algorithms for unchanged TIF is no longer suitable. The novel dwell time calculation method is needed to simultaneously consider the effect of multiple dwell points and tool path.

3.2. Tool path optimization

According to Section 3.1, the neighborhood effect is closely connected with the tool path type. In another word, the appropriate tool path may greatly simplify the existence of neighborhood effect, which can improve the feasibility of TIF changes compensation. In recent years, the existing

research of tool path mainly aims at suppressing the mid-spatial frequency (MSF) errors [23,24]. Generally, all the tool path types can be classified into two categories, raster path and non-raster path. Because of strong regularity, the periodic waviness unavoidably remains on the substrate surface while adopting the raster path. By contrast, the non-raster path with more randomness and multi-directionality, such as the pseudo-random paths and adaptive paths, presents the great advantages in the suppression of MSF errors. However, this process is not helpful to suppress the neighborhood effect in APPP, because the temperature changes are also randomized and become more uncontrollable. For example, there exist a large number of random inflection points in the random path shown in Fig. 3. In these positions, the velocity reduction occurs to change the motion direction, which leads to equivalent extra dwell time and further temperature rising. In this way, the TIF changes under neighborhood effect is more complex and diverse.

With the above analysis, we find that the raster path has a great potential in suppressing the neighborhood effect, precisely because of its regularity. In fact, the removal generation of raster path can be considered as the superposition of multiple one-dimensional (1D) velocity-variant trenches. Therefore, the neighborhood effect only exists in two forms, as shown in Fig. 4. First, the processing temperature at any dwell point is influenced by the dwell time combination of previous dwell points along the straight-line path [22], which can be called as 1D neighborhood effect, as shown in Fig. 4(a). Second, the neighborhood effect occurs between different velocity-variant trenches that are close to each other, as shown in Fig. 4(b). The first neighborhood effect only individually exists in the first 1D velocity-variant trench. In most cases, the two kinds of neighborhood effect are coupled together.
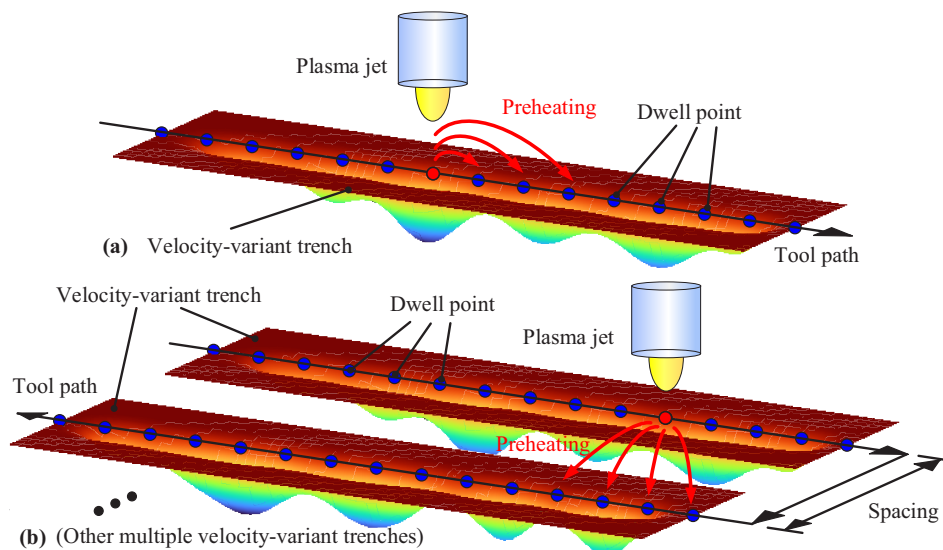

Fig. 4. Two forms of neighborhood effect in the raster path. (a) 1D neighborhood effect. (b) Neighborhood effect between different velocity-variant trenches.

To suppress the neighborhood effect, we noticed that the spacing value in raster path is extremely crucial to the complexity of temperature field. Generally, the small spacing is adopted in the conventional raster path, which makes the processing temperature changes of different trenches sensitive to each other. From another perspective, the larger spacing value can weaken the temperature interaction of different trenches. Further, if the spacing value is increased to a certain degree, the temperature interaction is expected to be thoroughly eliminated. Inspired by this, the multi-stagger raster path is presented in this paper to suppress the neighborhood effect, as shown in Fig. 5, which consists of the multiple conventional raster paths. Each of them adopts

the same larger spacing, but staggers each other with a small distance. In practical processing, every raster path is sequentially executed and achieve the targeting removal distribution together. Compared with the conventional raster path, the multi-stagger raster path is essentially acquired by optimizing the order of generating every 1D velocity-variant trench. The number of raster path execution n can be calculated as,

$$n = \frac{d}{L_s} \tag{6}$$

In Eq. (6), the larger spacing value is represented by d, which depends on technological parameters. Besides, L_s is the stagger distance. So far, the complex neighborhood effect only exists in one dimension, which improves the feasibility of compensating TIF changes.
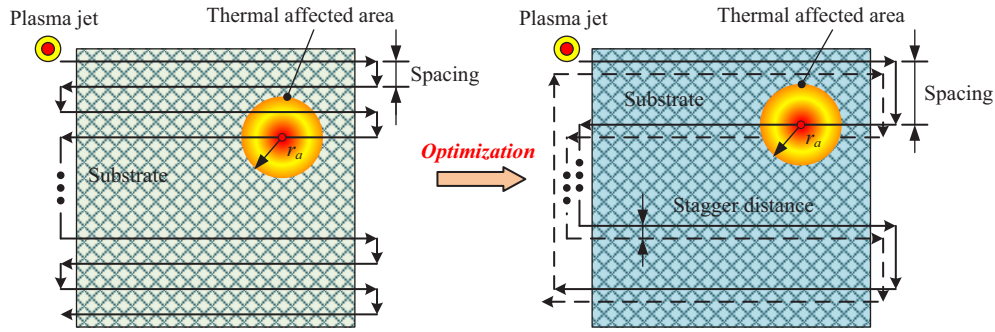

Fig. 5. Illustration of the multi-stagger raster path acquired by optimization.

3.3. Modeling of the TIF changes under 1D neighborhood effect

With the multi-stagger raster path, the 1D neighborhood effect becomes critical for precise control of two-dimensional (2D) removal generation. To achieve this, the TIF changes under 1D neighborhood effect should be accurately modeled. This indicates that the TIF calibration should be conducted by the velocity-variant trench experiment. Its necessity lies in the high consistency of neighborhood effect between the calibration and practical processing.

For any velocity-variant trench, its removal generation considering the neighborhood effect is described as,

$$E_{\text{practical}}(x) = R(x, T(x, t(x), t_1(x), t_2(x), \cdots, t_N(x))) \otimes t(x) \tag{7}$$

where N is the number of dwell points that contribute to the preheating effect. Considering the positive correlation, the processing temperature is mapped into dwell time, and Eq. (7) can be further modified as,

$$E_{\text{practical}}(x) = R(x, t(x), t_1(x), t_2(x), \cdots, t_N(x)) \otimes t(x) \tag{8}$$

In APPP, the typical removal profile can be perfectly fitted by the Gaussian curve [17]. Therefore, the multivariable time-variant TIF model can be established as,

$$R(x, t, t_1, t_2, \cdots, t_N) = a(t, t_1, t_2, \cdots, t_N) \cdot e^{-\frac{4\ln 2 x^2}{FWHM(t,t_1,t_2,\cdots,t_N)^2}} \tag{9}$$

where a is the peak removal rate and *FWHM* is the full width at half maximum. Although these two values can precisely describe the TIF changes, the volume removal rate (VRR) is the most essential and comprehensive. Based on this, Eq. (9) is transferred into,

$$Vrr(t, t_1, t_2, \cdots, t_N) = \frac{\pi}{4\ln 2} a(t, t_1, t_2, \cdots, t_N) \cdot FWHM(t, t_1, t_2, \cdots, t_N)^2 \tag{10}$$

To fully establish Eq. (10), the following two issues should be discussed by analyzing the influence factors of VRR. The first one is the influence of single dwell time on VRR, which can

be explained by the previous research [7,17]. There exists the exponential relationship between the removal rate (including a and *FWHM*) and dwell time. Therefore, the change of VRR also follows the same rule, which is described as,

$$f(t) = m_1 e^{m_2 t} + m_3 \tag{11}$$

The another one is how to describe the preheating contribution of each previous dwell point to the current dwell point, which is connected with the heating process of plasma jet. On the basis of prior knowledge, the preheating effect of previous dwell point is gradually weakened as the distance from the current dwell point increases. This is mainly attributed to the reduction of heat input from plasma jet, which is considered to be the Gaussian distribution. Therefore, the Gaussian decay function is defined to describe the changes of preheating contribution with the distance, as shown in Fig. 6.

$$g(p) = m_4 e^{-\frac{p^2}{2m_5^2}} \tag{12}$$

where p is the distance from the current dwell point to the previous dwell point. Based on the above analysis, the complete establishment of Eq. (10) can be conducted by combining Eq. (11) and Eq. (12).

$$Vrr(t_0, t_1, t_2, \cdots, t_N) = \sum_{i=0}^{N} g(p(i)) \cdot f(t_i) \tag{13}$$

For the consistency of describing the dwell points, t_0 is adopted in Eq. (13) to represent the current dwell point. The VRR values can be calculated by the reverse analysis method after the 1D velocity-variant trench experiment, which is developed to derive the practical TIF changes at every controlled dwell point from the practical removal [22].

$$S_{\text{practical}}(x, y) = \frac{t_{\text{practical}}(x, y) \cdot \int \int R_{\text{nominal}}(u, v) du dv}{t_{\text{nominal}}(x, y)} \tag{14}$$

where $R_{\text{nominal}}(u, v)$ is the stable TIF acquired by the single point experiment, and used to calculate $t_{\text{practical}}(x, y)$ by analyzing the experimental removal with the conventional dwell time algorithm. Besides, $t_{\text{nominal}}(x, y)$ is the executed 1D dwell time map. So far, the multivariable time-variant TIF model can be acquired by the nonlinear least-squares regression, which determines the five coefficients in Eq. (11) and (12).
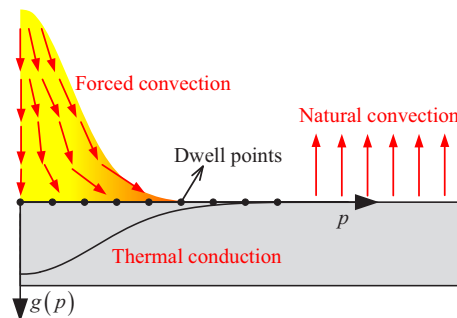

Fig. 6. Illustration of the Gaussian decay function.

3.4. Dwell time calculation method

The multivariable time-variant TIF model can comprehensively describe the TIF changes under neighborhood effect, but simultaneously make the conventional dwell time calculation method

invalid. So far, all the related algorithms focus on controlling the removal depth, where the calculated dwell time map should be verified by conducting the forward convolution. However, this idea cannot be extended for the multivariable time-variant TIF model, because the TIFs at each dwell point need to be fully described in the forward convolution. In APPP, this procedure can only be achieved by integrating the temperature-dependent TIF with calculation of temperature field, which is laborious and time-consuming.

In previous research, the concept of controlling LVR proposed by Su et al. [17] explained the removal generation in CCOS from another perspective. As long as the LVR is equal, different TIFs with different dwell time maps can achieve almost same removal distribution. This way, the removal generation with changed TIFs can be linked with the conventional CCOS procedure with unchanged TIF, which lays the theoretical foundation for the nonlinear dwell-time algorithm in APPP [21]. Based on this concept, it is not difficult to find that the LVR can also be adopted to evaluate the theoretical accuracy of calculated dwell time map. Besides, the multivariable time-variant TIF model describes the VRR changes, which is applicable for analyzing the accuracy of LVR. Its distinct advantage is the avoidance of convolution operation, which greatly saves the computational and memory cost.

The flowchart of dwell time calculation is given in Fig. 7, which is essentially an iterative procedure. Different from the conventional iterative deconvolution algorithm, the target is to achieve the desired LVR distribution, instead of the desired removal depth. Before conducting the iteration, the desired LVR distribution V_{desired} is determined by,

$$E(x, y) = R_{\text{unchanged}}(x, y) \otimes t_{\text{unchanged}}(x, y) \tag{15}$$

$$S_{\text{unchanged}} = \iint R_{\text{unchanged}}(x, y) dx dy \tag{16}$$

$$V_{\text{desired}}(x, y) = t_{\text{unchanged}}(x, y) \cdot S_{\text{unchanged}} \tag{17}$$

where Eq. (15) describes the deconvolution procedure with any conventional method. $S_{\text{unchanged}}$ represents the VRR of unchanged TIF $R_{\text{unchanged}}(x, y)$, which is corresponded with the dwell time map $t_{\text{unchanged}}(x, y)$. In this part, the iterative deconvolution method is recommended, because it can achieve the better smoothness and need lower computation cost, compared with the matrix method. To make the iteration begin, $t_{\text{unchanged}}(x, y)$ is adopted as the initial dwell time map $t_0(x, y)$.

In each iteration, the practical VRR distribution $S_{\text{predicted}}(x, y)$ is first predicted with the multivariable time-variant TIF model. It is worth noting that the multi-stagger raster path is of great importance in this procedure, because the neighborhood effect is directional. Therefore, the VRR prediction needs to be carried out individually in the left-to-right and right-to-left direction. Based on this, the predicted LVR distribution $V_{\text{predicted}}(x, y)$ can be further calculated by,

$$V_{\text{predicted}}(x, y) = S_{\text{predicted}}(x, y) \cdot t_k(x, y) \tag{18}$$

By comparing the desired and practical LVR distribution, the dwell time map in each iteration can be updated by,

$$t_{k+1}(x, y) = t_k(x, y) + \frac{V_{\text{desired}}(x, y) - V_{\text{practical}}(x, y)}{S_{\text{unchanged}}} \tag{19}$$

$$t_k(t_k \leq t_{\min}) = t_{\min} \tag{20}$$

$$t_k(t_k \geq t_{\max}) = t_{\max} \tag{21}$$

where $t_{\min}$ and $t_{\max}$ are connected with the computer numerical control (CNC) dynamics.
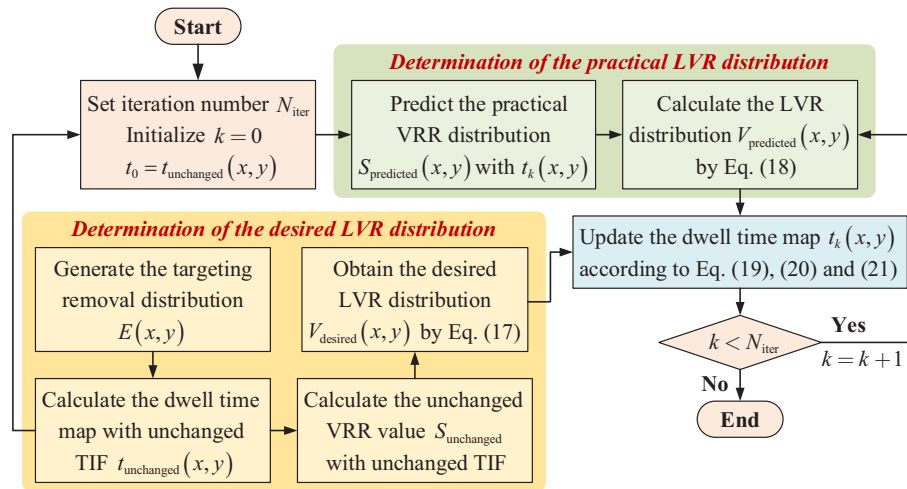
Fig. 7. Flowchart of the dwell time calculation.

4. Verification through simulation analysis

To verify the proposed methodology, the simulation analysis is conducted by combining the thermal model and processing. In practical, it is hard to implement the whole procedure in 2D case because of the unbearable computation cost. Considering the fundamentality, this section focuses on the 1D simulation analysis (not include the tool path), while the 2D case is verified through experiment in Section 5.

4.1. Simulation setup

Our previous research [22] has introduced the establishment of 1D thermal model to investigate the neighborhood effect, as shown in Fig. 8. It considers the thermal convection and conduction, which is respectively solved with Newton's law of cooling and Fourier's law. Besides, an explicit relationship between the temperature and the TIFs was also defined. This way, the value of a and *FWHM* can be calculated to fully describe the TIFs at each dwell point. With any dwell time map, the practical removal distribution considering temperature can be acquired by the forward convolution.
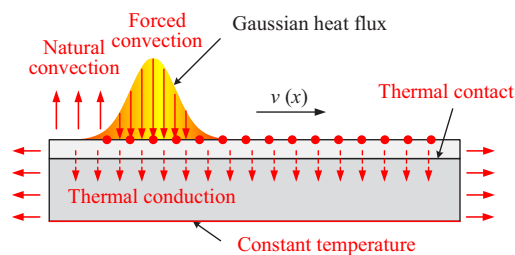

Fig. 8. Illustration of the established 1D thermal model [22].

The flowchart of the simulation analysis is illustrated in Fig. 9. First, the 1D dwell time map is defined to carry out the TIF calibration simulation. Then, the generated velocity-variant trench is extracted to calculate the VRR values by the reverse analysis [22]. Next, the nonlinear

least-squares regression is conducted to determine the five coefficients in the multivariable time-variant TIF model. The above analysis is discussed in Section 4.2. Based on this, the targeting removal distribution is generated, and the corresponding dwell time map can be calculated with the multivariable time-variant TIF model. Further, the practical removal distribution can be calculated with the thermal model, which is compared with the targeting removal distribution.
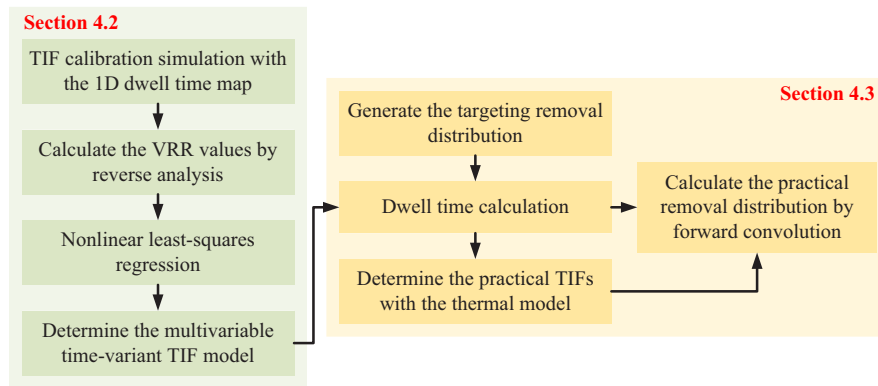

Fig. 9. Flowchart of the simulation analysis.

It should be noted that the selection of unchanged TIF in dwell time calculation should be checked in advance [21]. This make sure that the selected TIF is capable of achieving the accurate removal, and so is the desired LVR. Besides, the existing time-variant TIF model and its corresponding dwell time map are also analyzed simultaneously to compare with the proposed methodology.

4.2. Verification of the multivariable time-variant TIF model

In the TIF calibration simulation, the 1D sinusoidal dwell time map was defined to generate the velocity-variant trench, as shown in Fig. 10(a). The dwell points were assigned from 10 mm to 90 mm at the interval of 1 mm. The spatial wavelength, amplitude and minimum value were respectively 40 mm and 0.5 s, 0.1s, which is given in Fig. 10(b).
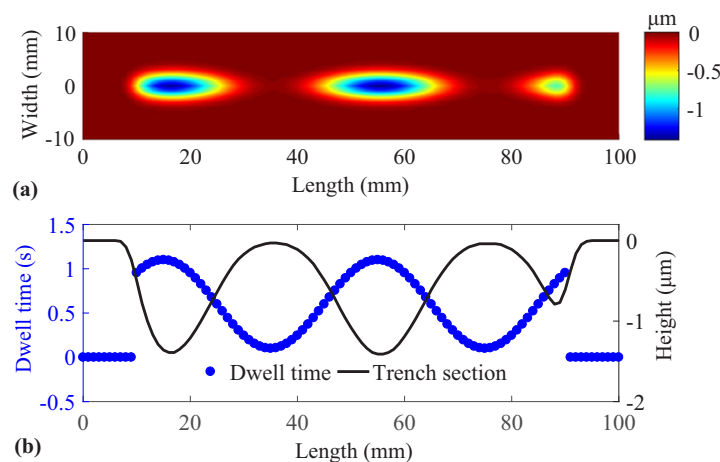

Fig. 10. Velocity-variant trench in the TIF calibration simulation. (a) Removal distribution. (b) Dwell time map and trench section.

Figure 11 gives the result of the nonlinear least-squares regression based on the VRR values calculated by the reverse analysis. In the regression stage, the value of N is determined to be 10 considering the heat flux distribution. Because of the edge effect in the reverse analysis [22], the calculated VRR values present the obvious abnormity in the edge area of dwell time map. However, this phenomenon does not influence the regression analysis, which can be overall matched with the calculated VRR values. Therefore, the regression error mainly comes from the edge effect in the reverse analysis, instead of the TIF model establishment. Finally, the established multivariable time-variant TIF model is determined to be,

$$Vrr(t_0, t_1, t_2, \cdots, t_N) = \sum_{i=0}^{N} 0.3674 \mathrm{e}^{-\frac{i^2}{2 \cdot 2.1821^2}} \cdot (-0.5547 \mathrm{e}^{-0.5808 t_i} + 0.5561) \tag{22}$$

Meanwhile, the existing time-variant TIF model is also established based on the simulated multiple scanning test, which is determined to be,

$$Vrr(t) = -0.5887 \mathrm{e}^{-0.7157 t} + 0.5823 \tag{23}$$
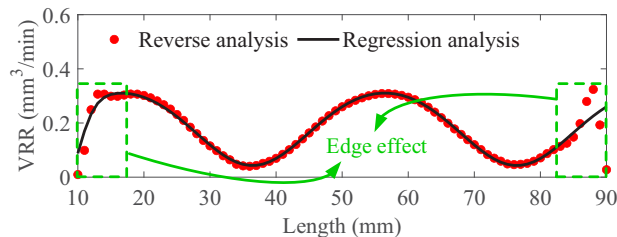

Fig. 11. Result of the nonlinear least-squares regression.

Based on the two different TIF models, the comparison between the practical and predicted VRR values is presented in Fig. 12. According to Fig. 12(a), the multivariable time-variant TIF model can perfectly predict the practical VRR values. As for the existing time-variant TIF model, the prediction error is mainly embodied by the phase deviation and peak-to-valley (PV) difference, as shown in Fig. 12(b), which has been fully analyzed in the previous research [22]. By contrast, this prediction error is fully eliminated in the multivariable time-variant TIF model. Besides, it is worth noting that the VRR collapse caused by insufficient heating is also simultaneously modeled. To characterize the prediction error, the ratio of the root mean square (RMS) of prediction error to the RMS of practical value is defined. This way, the prediction error is greatly reduced from 23.7% to 5.3% by adopting the proposed TIF model, which proves its reasonability and validity.

4.3. Verification of the dwell time calculation

Figure 13 gives the calculated results of the targeting removal distribution. To illustrate the advantage of the proposed compensation method, the targeting removal distribution is defined as 1D freeform surface, as shown in Fig. 13(a), which consists of multiple surface components with different spatial wavelength and amplitude. With the two TIF models, different dwell time maps are calculated and given in Fig. 13(b). For existing time-variant TIF model, the dwell time calculation is inevitably affected by the prediction error in Fig. 12(b). In the rising of dwell time along the processing direction, the predicted VRR values are larger than the practical VRR values without considering the neighborhood effect, while it is the opposite in the decline of dwell time. This way, the values of dwell time in these two areas are respectively insufficient and excessive. Therefore, the TIF changes under neighborhood effect can be compensated by respectively increasing and reducing dwell time in these areas. By comparing the two dwell
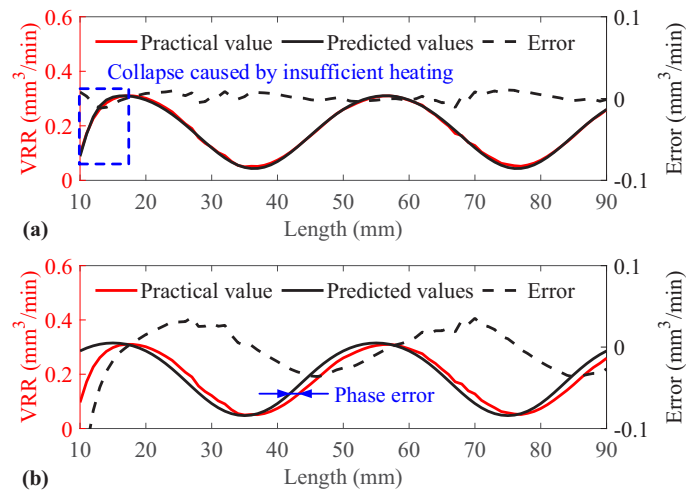
Fig. 12. Comparison between the practical (simulation) and predicted values by different TIF models. (a) Multivariable time-variant TIF model. (b) Existing time-variant TIF model.

time maps in Fig. 13(b), it is no doubt that their difference is consistent with the above analysis, and the dwell time map calculated by the multivariable time-variant TIF model can be expected to compensate the TIF changes under neighborhood effect. Further, the total processing times calculated by the existing and multivariable time-variant TIF model are respectively 71.2 s and 74.3 s. The value difference is mainly attributed to the extra compensation of VRR collapse caused by the insufficient heating at the beginning for the latter case. However, the difference of total processing time can be overall neglected, because the upward and downward adjustment of dwell time both occur simultaneously, as shown in Fig. 13(b).
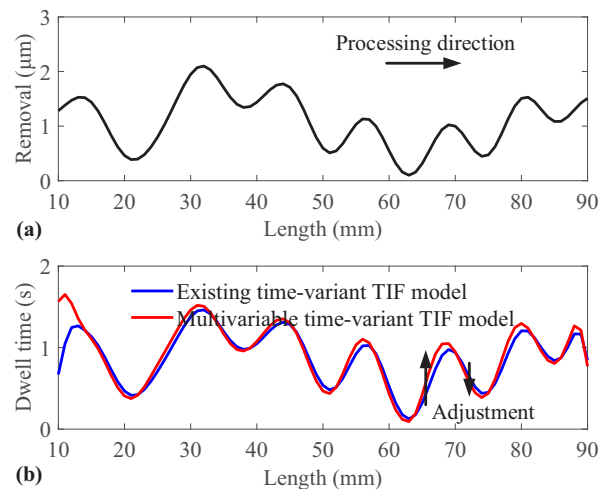

Fig. 13. Calculated results of the targeting removal distribution. (a) Targeting removal distribution. (b) Comparison of different dwell time maps.

Further, the practical removal distribution corresponding to the two dwell time maps are compared with the targeting removal distribution, which is presented in Fig. 14. With the multivariable time-variant TIF model, the calculated dwell time map is capable of achieving high

removal accuracy, as shown in Fig. 14(a). With the edge truncation, the convergence rate can reach up to 96.13%. By contrast, the large residual error is presented for the existing time-variant TIF model, as shown in Fig. 14(b). Compared with Fig. 12(b), it is obvious that the prediction error of the TIF model is transferred into the practical removal distribution. This phenomenon has also been discovered in the previous experimental research for neighborhood effect [22]. On this occasion, the theoretical convergence rate is only 86.67%.
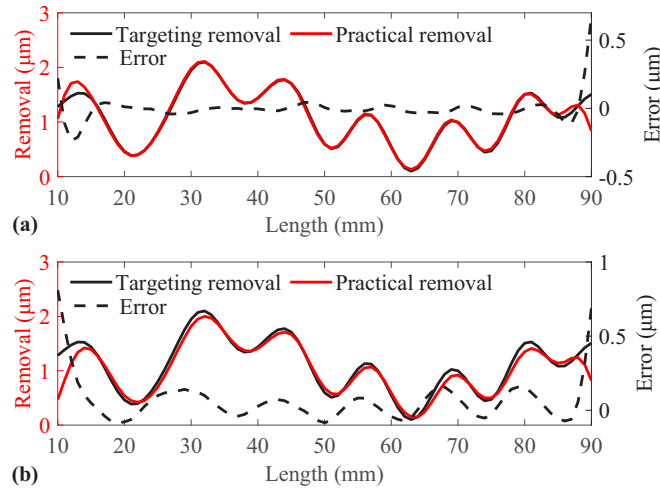

Fig. 14. Comparison between the practical and targeting removal distribution. (a) Multi-variable time-variant TIF model. (b) Existing time-variant TIF model.

The above simulation results proves that the proposed methodology is effective to compensate the TIF changes under neighborhood effect. Compared with the existing time-variant TIF model and its corresponding dwell time map, the proposed methodology can theoretically improve the convergence rate by nearly 10% without efficiency sacrifice.

5. Experimental validation

To verify the proposed methodology, the experimental validation was carried out in-house developed APPP machine, which is equipped with the low-power inductively coupled plasma (ICP) jet torch [25,26] as shown in Fig. 15. The working gases were Ar and CF_4, and the flow rates were 15 L/min and 30 mL/min. The plasma jet was excited at 380 W power. In this section, the continuous phase plate, as the freeform surface, was generated on a fused silica substrate in a single cycle of APPP, which indicated that the tool path optimization was included.

The targeting form error of freeform surface and its tool path design is given in Fig. 16. According to Fig. 16(a), the size of freeform surface is 80 mm×80 mm, and the PV and RMS of form error is respectively 1.52 μm and 241.8 nm. By preliminary experiment, it is found that the full width at half maximum of stable TIF is only 2.55 mm, and therefore the larger spacing value is determined to be 20 mm. Besides, the stagger distance is set to be 1 mm. This way, the raster path is executed 20 times in total, as shown in Fig. 16(b).

In the TIF calibration experiment, the spatial wavelength, amplitude and minimum value of adopted 1D sinusoidal dwell time map were 60 mm, 0.25 s and 0.1 s, as shown in Fig. 17(a). The processing length is 80 mm. By extracting the velocity-variant trench and conducting the reverse analysis, the VRR values of each dwell point is calculated, as shown in Fig. 17(b). With the nonlinear least-squares regression ($N = 10$), the multivariable time-variant TIF model is
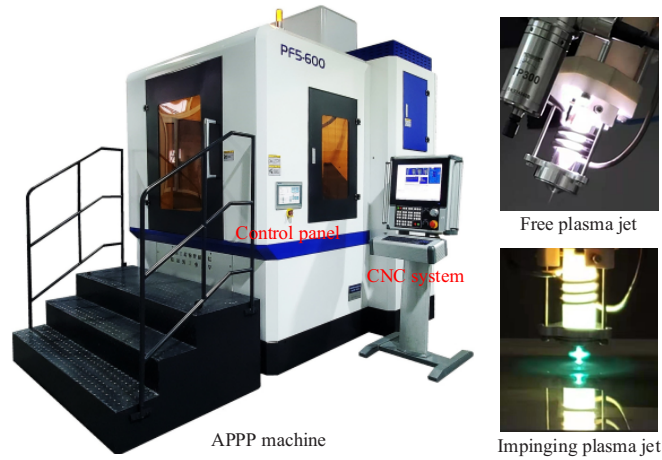
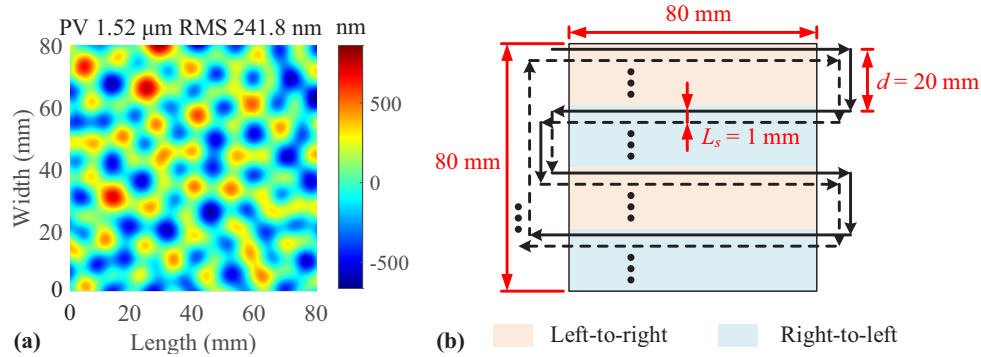**Fig. 15.** Experimental setup with our in-house developed APPP machine.

Fig. 16. Targeting form error and tool path design. (a) Form error distribution. (b) Tool path.

determined to be,

$$Vrr(t_0, t_1, t_2, \cdots, t_N) = \sum_{i=0}^{N} 0.4947 e^{-\frac{i^2}{2 \cdot 1.7876^2}} \cdot (-0.1051 e^{-3.5237 t_i} + 0.1342) \quad (24)$$

Aiming for the targeting form error given in Fig. 16, the dwell time is calculated with the calibrated TIF model and input to the CNC system to execute. It should be noted that the calculation procedure only needs 1.58 s, which shows the great efficiency advantages of the proposed method. The experimental results of the freeform surface are shown in Fig. 18. With the edge truncation to avoid edge effect, we only focus on the central range of 70 mm×70 mm, which is evaluated with the high-precision characterization method [27]. The corresponding designed surface is given in Fig. 18(a), and its RMS values is 244.5 nm. With only one cycle of APPP, the RMS values of processed surface is 260.5 nm, as shown in Fig. 18(b). Figure 18(c) presents the form error distribution, which indicates that the RMS value is only 40.2 nm. Therefore, the single convergence rate can be determined to be 83.6%. Therefore, the experimental results demonstrates that the proposed method in this paper can effectively compensate the TIF changes under neighborhood effect.
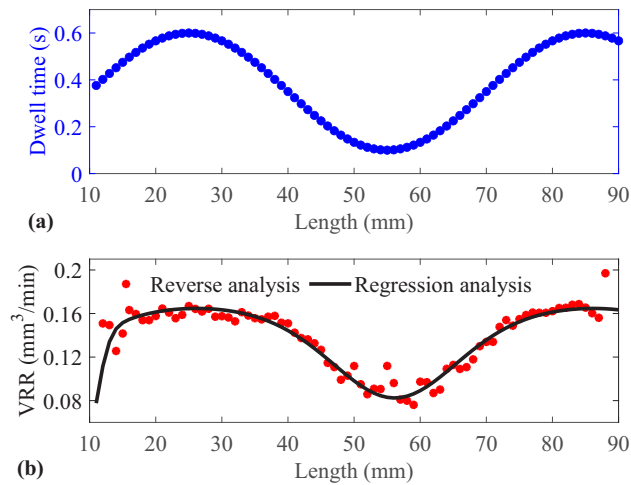
Fig. 17. Results of the TIF calibration experiment. (a) 1D sinusoidal dwell time map. (b) Reverse analysis and nonlinear least-squares regression.
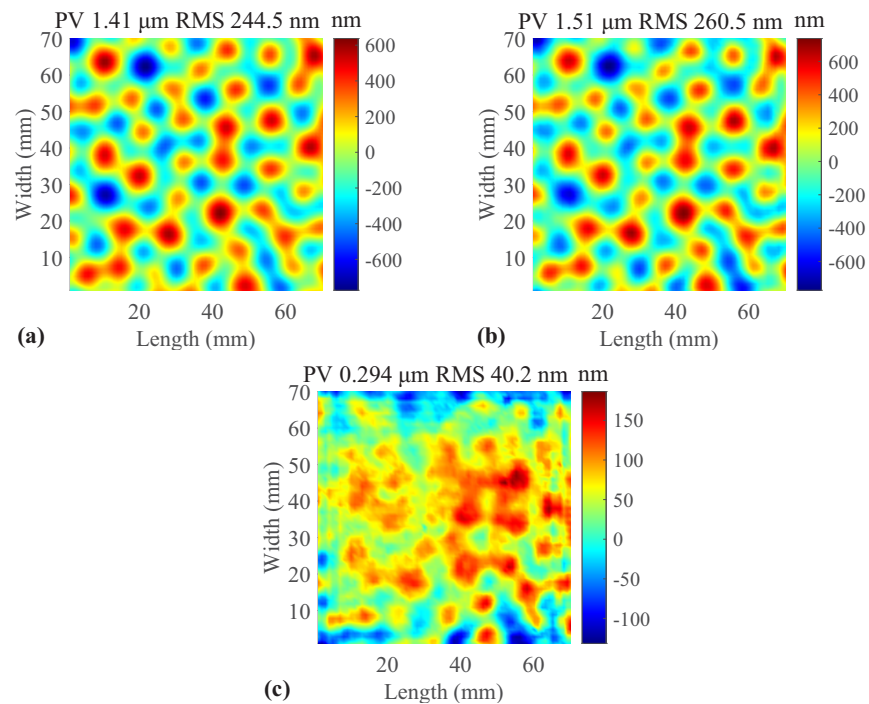

Fig. 18. Experimental results of the freeform surface. (a) Designed surface. (b) Processed surface. (c) Form error.

6. Conclusions

In this paper, the compensation of TIF changes under neighborhood effect in APPP is proposed, which serves for enhancing the removal controllability and improving the convergence rate of single processing. From the theoretical analysis, simulation and experimental results, the main conclusions and contributions of this paper are as follows:

(1) The temperature field during APPP is qualitatively analyzed, which makes it clear that the compensation of TIF changes should be conducted from three aspects. First, the multi-stagger raster path is proposed to suppress the complex neighborhood effect, which only exists in one dimension. Second, the multivariable time-variant TIF model is established to model the TIF changes under 1D neighborhood effect. Three, the corresponding dwell time calculation method is further developed.

(2) With the thermal model and defined temperature-dependent TIF, the simulation analysis was implemented to investigate the TIF model establishment and dwell time calculation. The results show that the prediction error of multivariable time-variant TIF model is only 5.3%, and the corresponding calculated dwell time map can achieve the theoretical convergence rate of 96.13%, with the neighborhood effect thermally considered.

(3) The experimental validation was carried out by the generation of complex freeform surface. With the proposed method, the high convergence rate of 83.6% is achieved under the significant neighborhood effect. Therefore, the results demonstrate that the proposed method is feasible and applicable to the compensation of the caused TIF changes.

Disclosures. The authors declare no conflicts of interest.

Data availability. Data underlying the results presented in this paper are not publicly available at this time but may be obtained from the authors upon reasonable request.

References

1. R. A. Jones, "Optimization of computer controlled polishing," Appl. Opt. **16**(1), 218–224 (1977).
2. A. Beaucamp, T. Katsuura, and K. Takata, "Process mechanism in ultrasonic cavitation assisted fluid jet polishing," CIRP Ann. **67**(1), 361–364 (2018).
3. J. Hou, M. Cao, H. Wang, H. Zhao, B. Zhong, Z. Jiang, and Y. Li, "Determination of optimized removal functions for imprinting continuous phase plates using fuzzy theory," Appl. Opt. **57**(21), 6089–6096 (2018).
4. M. Xu, Y. Dai, X. Xie, L. Zhou, and W. Peng, "Fabrication of continuous phase plates with small structures based on recursive frequency filtered ion beam figuring," Opt. Express **25**(10), 10765–10778 (2017).
5. D. D. Walker, D. Brooks, A. King, R. Freeman, R. Morton, G. McCavana, and S.-W. Kim, "The 'Precessions' tooling for polishing and figuring flat, spherical and aspheric surfaces," Opt. Express **11**(8), 958–964 (2003).
6. D. Li, P. Ji, Y. Xu, B. Wang, Z. Qiao, and F. Ding, "Development of computer-controlled atmospheric pressure plasma structuring for 2D/3D pattern on fused silica," Sci. Rep. **11**(1), 22392 (2021).
7. P. Ji, D. Li, X. Su, Z. Qiao, K. Wu, L. Song, B. Peng, and B. Wang, "Optimization strategy for the velocity distribution based on tool influence function non-linearity in atmospheric pressure plasma processing," Precis. Eng. **65**, 269–278 (2020).
8. M. Castelli, R. Jourdain, P. Morantz, and P. Shore, "Rapid optical surface figuring using reactive atom plasma," Precis. Eng. **36**(3), 467–476 (2012).
9. T. Arnold, G. Boehm, I.-M. Eichentopf, M. Janietz, J. Meister, and A. Schindler, "Plasma Jet Machining," Vak. Forsch. Prax. **22**(4), 10–16 (2010).
10. Y. Mori, K. Yamauchi, K. Yamamura, and Y. Sano, "Development of plasma chemical vaporization machining," Rev. Sci. Instrum. **71**(12), 4627–4632 (2000).
11. B. Shi, Y. Dai, X. Xie, S. Li, and L. Zhou, "Arc-Enhanced Plasma Machining Technology for High Efficiency Machining of Silicon Carbide," Plasma Chem. Plasma Process. **36**(3), 891–900 (2016).
12. H. Jin, Q. Xin, N. Li, J. Jin, B. Wang, and Y. Yao, "The morphology and chemistry evolution of fused silica surface after Ar/CF4 atmospheric pressure plasma processing," Appl. Surf. Sci. **286**, 405–411 (2013).
13. L. Li, L. Zheng, W. Deng, X. Wang, X. Wang, B. Zhang, Y. Bai, H. Hu, and X. Zhang, "Optimized dwell time algorithm in magnetorheological finishing," The International Journal of Advanced Manufacturing Technology **81**(5-8), 833–841 (2015).
14. T. Wang, L. Huang, M. Vescovi, D. Kuhne, K. Tayabaly, N. Bouet, and M. Idir, "Study on an effective one-dimensional ion-beam figuring method," Opt. Express **27**(11), 15368–15381 (2019).
15. B. Zhong, W. Deng, X. Chen, S. Wen, J. Wang, and Q. Xu, "Frequency division combined machining method to improve polishing efficiency of continuous phase plate by bonnet polishing," Opt. Express **29**(2), 1597–1612 (2021).
16. T. Wang, L. Huang, M. Vescovi, D. Kuhne, Y. Zhu, V. S. Negi, Z. Zhang, C. Wang, X. Ke, H. Choi, W. C. Pullen, D. Kim, Q. Kemao, K. Nakhoda, N. Bouet, and M. Idir, "Universal dwell time optimization for deterministic optics fabrication," Opt. Express **29**(23), 38737–38757 (2021).

17. X. Su, P. Ji, Y. Jin, D. Li, Z. Qiao, F. Ding, X. Yue, and B. Wang, "Freeform surface generation by atmospheric pressure plasma processing using a time-variant influence function," Opt. Express **29**(8), 11479–11493 (2021).

18. C. Shi, C. Wang, C. F. Cheung, Z. Zhang, Z. Li, L. T. Ho, W. Deng, and X. Zhang, "Curvature effect-based modeling and experimentation of the material removal in polishing optical surfaces using a flexible ball-end tool," Opt. Express **30**(14), 24611–24638 (2022).

19. J. Zhang and H. Wang, "Generic model of time-variant tool influence function and dwell-time algorithm for deterministic polishing," Int. J. Mech. Sci. **211**, 106795 (2021).

20. J. Meister and T. Arnold, "New Process Simulation Procedure for High-Rate Plasma Jet Machining," Plasma Chem. Plasma Process. **31**(1), 91–107 (2011).

21. X. Su and X. Yue, "Nonlinear dwell-time algorithm for freeform surface generation by atmospheric-pressure plasma processing," Opt. Express **30**(11), 18348–18363 (2022).

22. P. Ji, D. Li, X. Su, Y. Jin, Z. Qiao, B. Wang, and F. Ding, "Investigation of the tool influence function neighborhood effect in atmospheric pressure plasma processing based on an innovative reverse analysis method," Opt. Express **29**(20), 31376–31392 (2021).

23. K. Takizawa and A. Beaucamp, "Comparison of tool feed influence in CNC polishing between a novel circular-random path and other pseudo-random paths," Opt. Express **25**(19), 22411–22424 (2017).

24. Z. Dong and W. Nai, "Surface ripple suppression in subaperture polishing with fragment-type tool paths," Appl. Opt. **57**(19), 5523–5532 (2018).

25. Y. Jin, X. Su, B. Wang, D. Li, F. Ding, and Z. Qiao, "The design and analysis of a novel low power atmospheric plasma jet torch for optical fabrication," J. Manuf. Processes **69**, 422–433 (2021).

26. Y. Jin, B. Wang, P. Ji, Z. Qiao, D. Li, and F. Ding, "Jet shape analysis and removal function optimization of atmospheric plasma processing applied in optical fabrication," The International Journal of Advanced Manufacturing Technology **120**(7-8), 5325–5338 (2022).

27. P. Ji, B. Wang, D. Li, Y. Jin, F. Ding, and Z. Qiao, "Analysis of the misalignment effect and the characterization method for imprinting continuous phase plates," Opt. Express **29**(11), 17554–17572 (2021).